



Insight into the superior piezophotocatalytic performance of BaTiO₃//ZnO Janus nanofibrous heterostructures in the treatment of multi-pollutants from water

He Lv^a, Yanan Liu^{a,*}, Ping Zhao^a, Yubin Bai^a, Wenxin Cui^{a,b}, Shuling Shen^a, Yang Liu^c, Zheng Wang^{b,*}, Deng-Guang Yu^{a,*}

^a School of Materials & Chemistry, University of Shanghai for Science and Technology, 516 Jungong Road, Shanghai 200093, China

^b Shanghai Institute of Ceramics, Chinese Academy of Sciences, Shanghai 201899, China

^c School of Chemistry and Chemical Engineering, Shanghai University of Engineering Science, 333 Long Teng Road, Shanghai 201620, China

ARTICLE INFO

Keywords:

Piezophotocatalysis
BTO//ZO Janus nanofibers membrane
Multi-pollutants degradation
Ni²⁺ and Cu²⁺ adsorption

ABSTRACT

Piezophotocatalytic technology has emerged as a promising wastewater treatment approach recently. A novel piezoelectric material, the flexible bamboo-like BaTiO₃//ZnO Janus nanofibers membrane (BTO//ZO JNM), was fabricated via side-by-side electrospinning. The as-prepared BTO//ZO JNM exhibited superior durability and universal applicability in the removal of bisphenol A, congo red, methylene blue and tetracycline hydrochloride under stir and light irradiation. The removal of these pollutants reached 94.75%, 93.45%, 99.06% and 97.65% within 60 min, respectively. The adsorption of Ni²⁺ and Cu²⁺ and their effects on catalytic degradation were also studied. Importantly, owing to the significantly raising macroscopic polarization, BTO//ZO JNM possessed higher degradation efficiency than that of uniaxial blend nanofibrous membrane, which was illustrated by COMSOL simulation. An in-depth understanding of piezophotocatalysis mechanism was speculated through construction-performance relationships of Janus heterojunction. This BTO//ZO JNM process will provide a new strategy for the development of piezoelectric materials for the treatment of mixed pollutants.

1. Introduction

With the expansion of industrialization and human activities in recent years, water pollution has become the most important problem faced by our planet. In particular, the widespread use of organics and heavy metals has caused extensive and severe harm to human health and living beings [1–3]. Compared with simple molecular pollutants, these sewages with complex components are more difficult to decompose due to the complexation between them, and the adsorption and oxidation processes of organic pollutants are changed. Therefore, the efficient removal of coexisting organic compounds and inorganic heavy-metal ions in wastewater has attracted the attention of many researchers.

Among the various water treatment technologies, advanced oxidation technology [4–7] is a cheap and environmentally-friendly technology. It uses oxidative active free radicals to degrade pollutants in water into non-toxic products. Even though solar-powered photocatalytic oxidation has been widely used to treat water sources, it still suffers from low quantum efficiency, difficult catalyst design, and a lack

of reactivity in the absence of solar irradiation. Piezophotocatalysts have brought “light” to photocatalysts. They can utilize ubiquitous mechanical force, such as pressure [8], shear force [9], stir [10], ultrasound [11], and thermal energy [12], to degrade organic pollutants. Under mechanical forces, electrons and holes on the surfaces of piezoelectric catalysts are separated, and redox reactions are stimulated to produce active free radicals and finally degrade pollutants in water. Therefore, the application of piezophotocatalysts is considered as a new method for gathering and using numerous ambient energy sources. Among numerous mechanical forces, stir has the lowest energy consumption. Moreover, it can simulate the flow of water, which is easy to realize in nature. Therefore, stir is considered to have the greatest potential for degradation.

Currently, there are several piezoelectric materials that could function as piezophotocatalysts, such as BaTiO₃ (BTO) [13], ZnO (ZO) [14], BiOX (Cl, Br, I) [15], KNbO₃ [16], NaNbO₃ [17], MoS₂ [18], BiVO₄ [19], ZnSnO₃ [20], Bi₂WO₆ [21], and Bi₄Ti₃O₁₂ [22]. The performances of these piezoelectric materials are mainly dependent on their morphology

* Corresponding authors.

E-mail addresses: yananliu@usst.edu.cn (Y. Liu), wangzheng@mail.sic.ac.cn (Z. Wang), ydg017@usst.edu.cn (D.-G. Yu).

<https://doi.org/10.1016/j.apcatb.2023.122623>

Received 17 November 2022; Received in revised form 10 March 2023; Accepted 11 March 2023

Available online 13 March 2023

0926-3373/© 2023 Elsevier B.V. All rights reserved.

and structure [23], metal, carbon doping [24,25] and lattice arrangement [26]. For example, tetragonal BTO exhibits a higher dielectric constant and piezoelectric coefficient (d_{33} of 45 pC/N) due to its divergence of the positive and negative centers [27], but its electron transport ability is relatively lower. Compared with other piezoelectric materials, noncentrosymmetric ZO has higher electron mobility and high piezoelectric coefficient; in particular, the piezoelectric coefficient of hexagonal wurtzite ZO can reach 125 pC/N [28]. They are all good candidate materials for piezophotocatalysis. Nevertheless, the construction of heterostructures that can be also considered as Janus heterostructures is the most efficient method. A number of studies have indicated that Janus heterostructures can be built on the basis of the internal electric field of the n-n heterojunctions to achieve the rapid and complete degradation of organic pollutants, promote charge transfer, and prevent the recombination of electron-hole pairs by ultrasonic activation. These Janus heterostructures materials include BiOI/ZO [11], $\text{Bi}_2\text{MoO}_6/\text{BiOBr}$ [29], BTO/ $\text{La}_2\text{Ti}_2\text{O}_7$ [30], $\text{PbTiO}_3/\text{TiO}_2$ [31], $\text{KNbO}_3/\alpha\text{-Fe}_2\text{O}_3$ [32], ZO/CdS [33], ZO/ MoS_2 [34], and others [35,36]. These materials all improve piezocatalytic activity by constructing Janus heterostructures. Furthermore, compared with ordinary single materials, Janus heterostructures exhibit better properties, including higher catalytic oxidation ability for degrading sewage and other kinds of pollutants [17,34], higher catalytic activity given that both of their sides can be directly exposed, and better stability in catalytic reaction because one side of them is wrapped by another material. Thus, it is important to prepare Janus heterostructures materials to improve piezophotocatalytic performance.

Janus nanofibers membranes (JNMs), which benefit from the structural advantages of Janus heterojunctions, can effectively avoid the unfavorable factor of the centrosymmetric localization of the plasmonic near-fields [37] generated by Janus heterojunctions. Such a characteristic structure provides important guidance for further improving the performance of materials. Recently, JNMs have been utilized in photocatalysis [4], wound dressings [38] and anti-bacteria applications [39]. JNMs can be fabricated by using the one-pot side-by-side electrospinning method. This technology is straightforward and simple to use, and its settings can be changed as needed [38–40]. The composition of the membrane, which is the template used to prepared JNMs, can tailor in accordance with the application of JNMs. This property is of great importance for future practical applications. More importantly, a contact surface is formed between two parallel nanofibers that can prevent the centrosymmetric localization of the plasmonic near-fields and is conducive to catalytic reactions. Finally, JNMs can also effectively prevent the recombination of electrons and holes in composite materials.

Given the aforementioned, classical BTO and ZO are selected as materials with piezophotocatalytic and adsorption characteristics. BTO//ZO Janus nanofibers membrane (BTO//ZO JNM) with bamboo-like structure is fabricated by using the one-pot side-by-side electrospinning technique. Finite element simulation reveals that the elaborately constructed Janus nanofibrous heterostructures have better piezoelectric performance than uniaxial blend nanofibrous membranes. The piezoelectric performance of BTO//ZO JNM is estimated by piezoresponse force microscopy (PFM). In the treatment of water pollutants with complex components, the BTO//ZO JNM will be applied to remove various metal ions and organic contaminants, which are close to the actual wastewater system. The adsorption of Ni^{2+} and Cu^{2+} as well as their effects on the catalytic degradation of several contaminants are also studied. The mechanical and cycling properties of flexible JNM are further evaluated to fully realize the piezophotocatalytic degradation of pollutants. Furthermore, this work offers a practical and environmentally friendly approach for the use and application of stir-induced piezophotocatalytic degradation of several contaminants. It has established some theoretical groundwork for ongoing research in science and its practical applications.

2. Materials and methods

2.1. Materials

BTO (99.9%, metals basis, $<3\ \mu\text{m}$), ZO (99.9%, $50 \pm 10\ \text{nm}$), polyvinylpyrrolidone (PVP, $M_w = 360\ 000$), polyvinylidene fluoride (PVDF, $M_w = 400\ 000$), potassium bromide (KBr, SP), potassium chloride (KCl, 99.5%), sodium sulfate (Na_2SO_4 , 99%), methylene blue (MB), tetracycline hydrochloride (TC, USP), BPA ($>99.0\%$), congo red (CR), *N,N*-dimethylformamide (DMF, AR, 99.5%) and BaSO_4 (SP) were purchased from Macklin. Acetone (AR, $\geq 99.5\%$) and hydrochloric acid (HCl, AR, purity $\approx 36\%–38\%$) were provided by Sinopharm Chemical Reagent Co., Ltd. (Shanghai, China). Deionized water was homemade. All reagents were of analytical grade and used without further purification.

2.2. Preparation of BTO//ZO JNM

The preparation process of BTO//ZO JNM is illustrated in Fig. S1. First, 1.12 g of PVDF and 0.56 g of PVP were dissolved in the mixture of acetone (6 mL) and DMF (8 mL). The mixture was heated at $60\ ^\circ\text{C}$ and stirred for 4 h until homogeneous. Next, a certain amount of BTO nanoparticles (NPs) was added into the above mixture. The resulting solution was named as S1. ZO solution was prepared in a manner similar to S1 and named as S2. A specially made needle (Fig. S1) was used to prepare BTO//ZO JNM. S1 and S2 were placed in two syringes, respectively. Electrospinning was performed under a direct current of 12 kV for 10 h. The electrospinning distance was 15 cm. The pump rate was $1\ \text{mL h}^{-1}$. Tin was used as the collector. BTO//ZO JNM was peeled from the tin for the experiment. Other samples were prepared to highlight the advantages of BTO//ZO JNM in piezophotocatalysis. The compositions and abbreviations of all the samples are shown in Table S1.

2.3. Material characterization, adsorption and piezophotocatalytic activity tests

The membranes were characterized by many techniques which were described in the supporting information (SI). The detailed adsorption and piezophotocatalytic activity tests were elucidated in the SI.

3. Results and discussion

3.1. Morphological and structural characterization

PVDF is recognized as the most suitable candidate polymer for the preparation of nanofiber membrane materials with piezoelectric property and is frequently used as an anti-fouling and anti-bacterial material [41,42], organic pollutants [43], and sensor [44]. However, pure PVDF membranes require the addition of piezoelectric materials due to their relatively low piezoelectric characteristics. In this research, the classical piezoelectric materials BTO and ZO NPs were added to enhance the piezoelectric performance. The PVDF/PVP nanofibers membrane, except for the membrane with the mixing ratio of PVDF/PVP is 2:1 (Fig. S2), had a uniform diameter of nanofibers. The diversity of nanofibers diameter may be ascribed to the low PVDF contents. Interestingly, the Janus nanofibers exhibit a bamboo-like structure and high PVDF contents may induce PVP aggregation (Fig. S2c) [45]. The addition of BTO and ZO NPs increase the roughness of the surface morphology of the above structure, as illustrated in Fig. 1b. 2% BTO//ZO JNM has diameter of $0.6957 \pm 0.03628\ \mu\text{m}$ and a significantly increased BET surface area as depicted in Fig. S3. Given that different kinds of polymers are easy to separate, the BET surface area of JNM significantly increased with the addition of PVP [46]. For comparison, BTO/ZO NM was also prepared (Fig. 1a). The nanofibers in BTO/ZO NM has a similar morphology as 2% BTO//ZO JNM, but a slightly lower diameter of $0.5203 \pm 0.02534\ \mu\text{m}$.

The TEM image of the characteristic Janus structure of 2% BTO//ZO

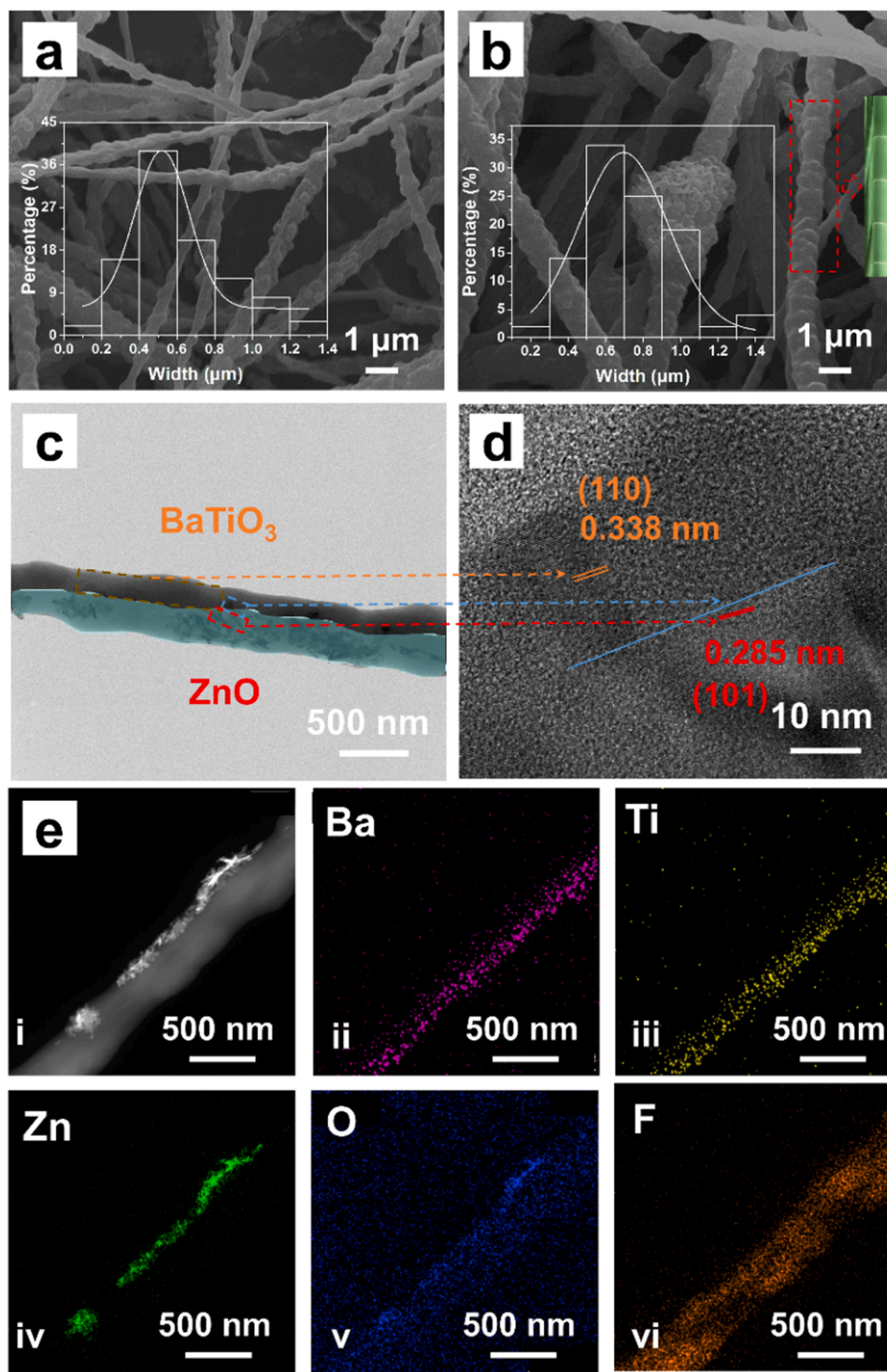


Fig. 1. SEM images of BTO/ZO NM (a) and 2% BTO//ZO JNM (b); TEM image of 2% BTO//ZO JNM (c); magnification of 2% BTO//ZO JNM (d); EDS mapping images of 2% BTO//ZO JNM (e) and the corresponding EDS elemental maps of Ba, Ti, Zn, O and F.

JNM is provided in Fig. 1c. The blue region in the nanofiber is the ZO side, which contained ZO NPs with diameters of 50 nm. The other region is the BTO side. EDS mapping images (Fig. 1e) clearly show that the distribution of the Ba and Ti are locally confined in one side of the Janus nanofibers, while the Zn is uniformly distributed in the other side of Janus nanofiber, O and F elements are distributed throughout the whole nanofiber. These results demonstrate that the Janus heterostructured nanofibers had been successfully synthesized through electrospinning. High-resolution TEM was performed to determine the crystallography of

2% BTO//ZO JNM (Figs. 1c and 1d). It reveals that the interplanar spacing of the NPs is 0.285 nm, which matched well with the (101) plane of hexagonal ZO. The latticing fringe of 0.338 nm is corresponded to the (110) plane of BTO. The marked blue line shows the contact interface between ZO and BTO. Previously reported Janus nanofibers easily separated from two fluids in the early stage of Taylor cone formation, thus limiting the formation of Janus nanofibers [47]. Therefore, we propose a new needle for the fabrication of Janus nanofibers to overcome the above limitation. JNM preparation through the

side-by-side electrospinning technique is controllable, and its parameters are easy to control.

The piezoelectric property of 2% BTO//ZO JNM was confirmed through PFM. The phase and amplitude images of 2% BTO//ZO JNM are provided in Fig. 2. 2% BTO//ZO JNM exhibits phases with different morphologies, indicating that the polarization directions in 2% BTO//ZO JNM differ (Fig. 2a). The clear differences in the amplitude of 2% BTO//ZO JNM (Fig. 2b) demonstrate that randomly distributed ferroelectric domains are present in 2% BTO//ZO JNM. The phase inversion of 2% BTO//ZO JNM is close to 180° after the voltage reversal of 10 V (Fig. 2c). This result indicates that 2% BTO//ZO JNM experiences local switching of ferroelectric polarization. Fig. 2d shows a clear “butterfly” amplitude loop for 2% BTO//ZO JNM. These results prove that 2% BTO//ZO JNM possesses excellent ferro/piezoelectric properties [25].

The crystalline structures of BTO NM, ZO NM and BTO//ZO JNM were characterized by XRD. The results of them are presented in Fig. 3a. The diffraction peaks of BTO NM correspond to those of the highly crystalline tetragonal phase BTO (PDF# 05-0626). The diffraction peaks of ZO NM can be indexed to hexagonal phase ZO (PDF# 36-1451 [48] and PDF# 97-3380). It can be seen that ZO exhibits the diffraction peaks at 31.8° (100), 34.4° (002), 36.3° (101), 47.5° (102), 56.6° (110), 62.9° (103), 66.4° (200), 68.0° (112), 69.1° (201), 72.6° (004), 77.0° (202), 81.4° (104), 90.0° (203) corresponding to PDF# 36-1451. And the diffraction peaks at 32.4° (100), 34.8° (002), 37.0° (101), 48.3° (102), 57.9° (110), 63.8° (103), 67.9° (200) and 69.3° (112) are corresponding to PDF# 97-3380. The two phases of PDF# 36-1451 and PDF# 97-3380 for ZO are similar, as shown in Fig. S4. The planes ((100), (002), (101), (102), (110), (103), (200), (112)) at 30° – 70° and the space group (P63mc) of them are same. Except for the cell volume is 47.62 \AA^3 and 45.3 \AA^3 , respectively. Tetragonal phase BTO and hexagonal phase ZO possess excellent piezophotocatalytic performance. The identified peaks of BTO//ZO JNM that are marked with red rectangles and blue dots are ascribed to the tetragonal phase BTO and hexagonal phase ZO, respectively. These results confirm that the BTO//ZO JNM had been

successfully synthesized as verified by TEM imaging. The diffraction peaks of BTO, ZO NM, and BTO//ZO JNM at around 20° are respectively corresponded to α -phase and β -phase of PVDF [49] and PVP [38].

XPS was used to analyze the surface compositions and chemical states of the elements in 2% BTO//ZO JNM, after adsorbing Ni^{2+} and Cu^{2+} . Their XPS spectra are shown in Fig. 3b. C, N, Ti, O, F, Ba, and Zn peaks are present in 2% BTO//ZO JNM. The XPS results are consistent with the XRD findings. These results indicate that 2% BTO//ZO JNM possesses numerous oxygen and nitrogen functional groups, the diffraction peak at 860.5 eV in 2% BTO//ZO JNM that comes into contact with Ni^{2+} is ascribed to Ni 2p, indicating that Ni^{2+} has been adsorbed [50]. Similarly, the diffraction peak of Cu 2p emerges at 932.6 eV, confirming that Cu^{2+} has been adsorbed by 2% BTO//ZO JNM [51]. The binding energies at 88.1 eV and 176.1 eV corresponded to Ba $4d^5$ and Ba $4p^3$, respectively [52].

Fig. S5a shows the Raman spectrum of 2% BTO//ZO JNM. The band located at 2974 cm^{-1} is ascribed to $-\text{CH}_2-$ symmetric stretching which is associated with β phase PVDF [43]. Given that the peaks of BTO, ZO NPs and PVDF at 3000 – 5000 cm^{-1} overlapped, FTIR must be used to measure the piezoelectric phase in PVDF, as presented in Fig. S5b and S5c. The peaks at 1276 and 1431 cm^{-1} characterize the piezoelectric β -phase PVDF. The peaks at 841 , 510 , and 841 cm^{-1} are characteristic peaks of β - and γ -phase PVDF. The peaks of α -, β - and γ -phase PVDF are at 881 , 1072 , 1182 , and 1403 cm^{-1} . Calculations reveal that the ratio of α -, β - and γ - phases PVDF in 2% BTO//ZO JNM were 6.40%, 90.63%, and 2.97%, respectively [43]. The detailed calculation processes were listed in SI. These results prove that piezoelectric PVDF had been successfully prepared through the electrospinning technique. The clear absorption band at 500 cm^{-1} in the spectra could be attributed to the BTO and ZO vibration [53,54]. Comparison with the FTIR spectrum of 2% BTO//ZO JNM reveals that some absorption peaks in the FTIR spectra have negligibly changed after Ni^{2+} and Cu^{2+} adsorption by 2% BTO//ZO JNM. For example, the absorption peaks of N–H and O–H at 3428 and 3250 cm^{-1} gradually disappear from the spectra of the samples likely

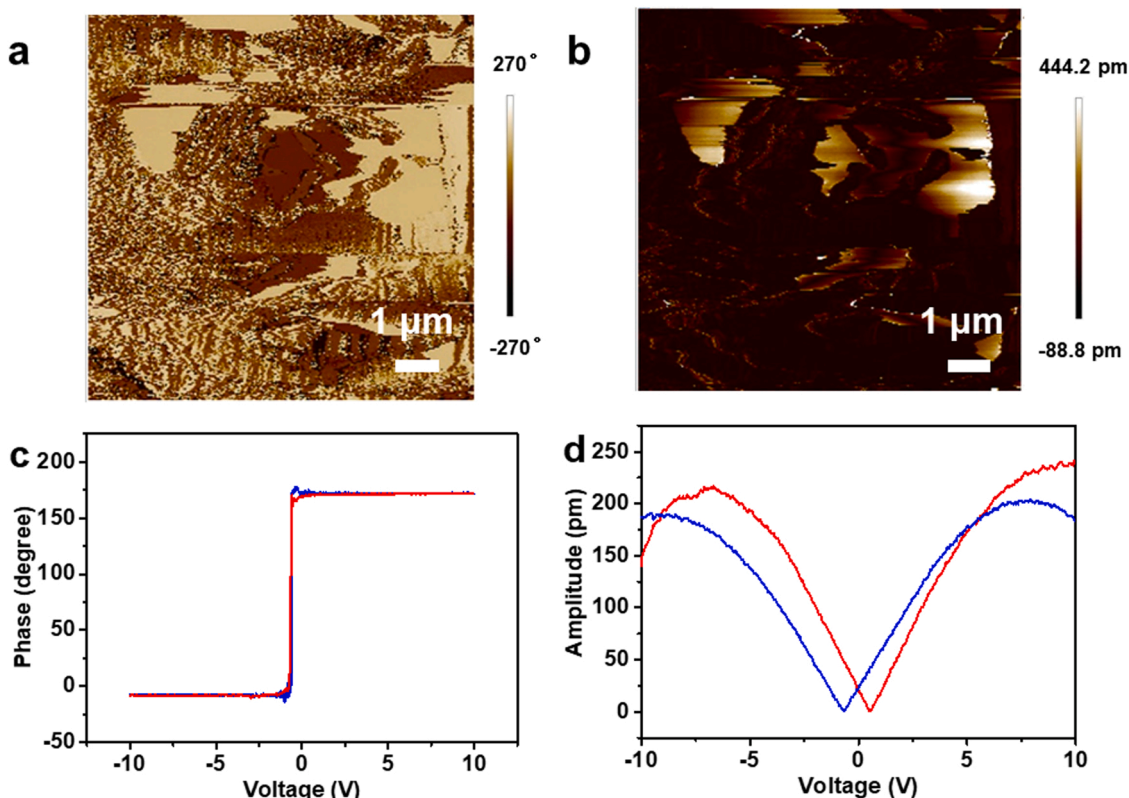


Fig. 2. Relative phase (a) and amplitude (b) of the piezoelectric response, phase hysteresis loop (c) and amplitude butterfly loop of 2% BTO//ZO JNM (d).

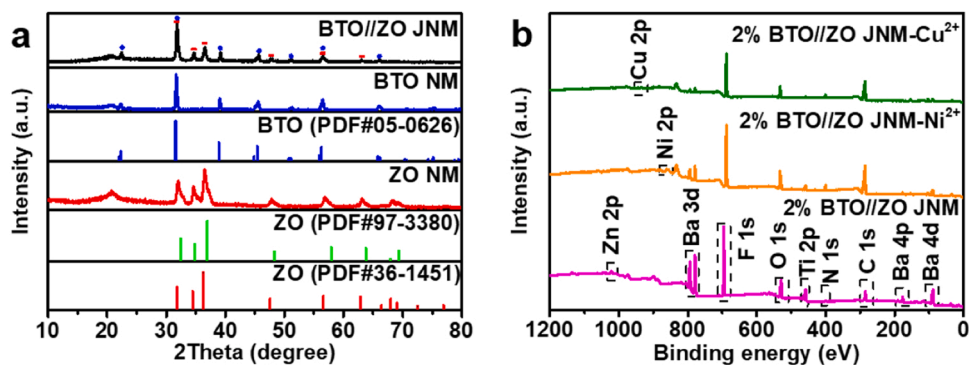


Fig. 3. XRD patterns of different samples (a), XPS survey spectra of 2% BTO//ZO JNM and 2% BTO//ZO JNM after adsorbing Ni^{2+} and Cu^{2+} (b).

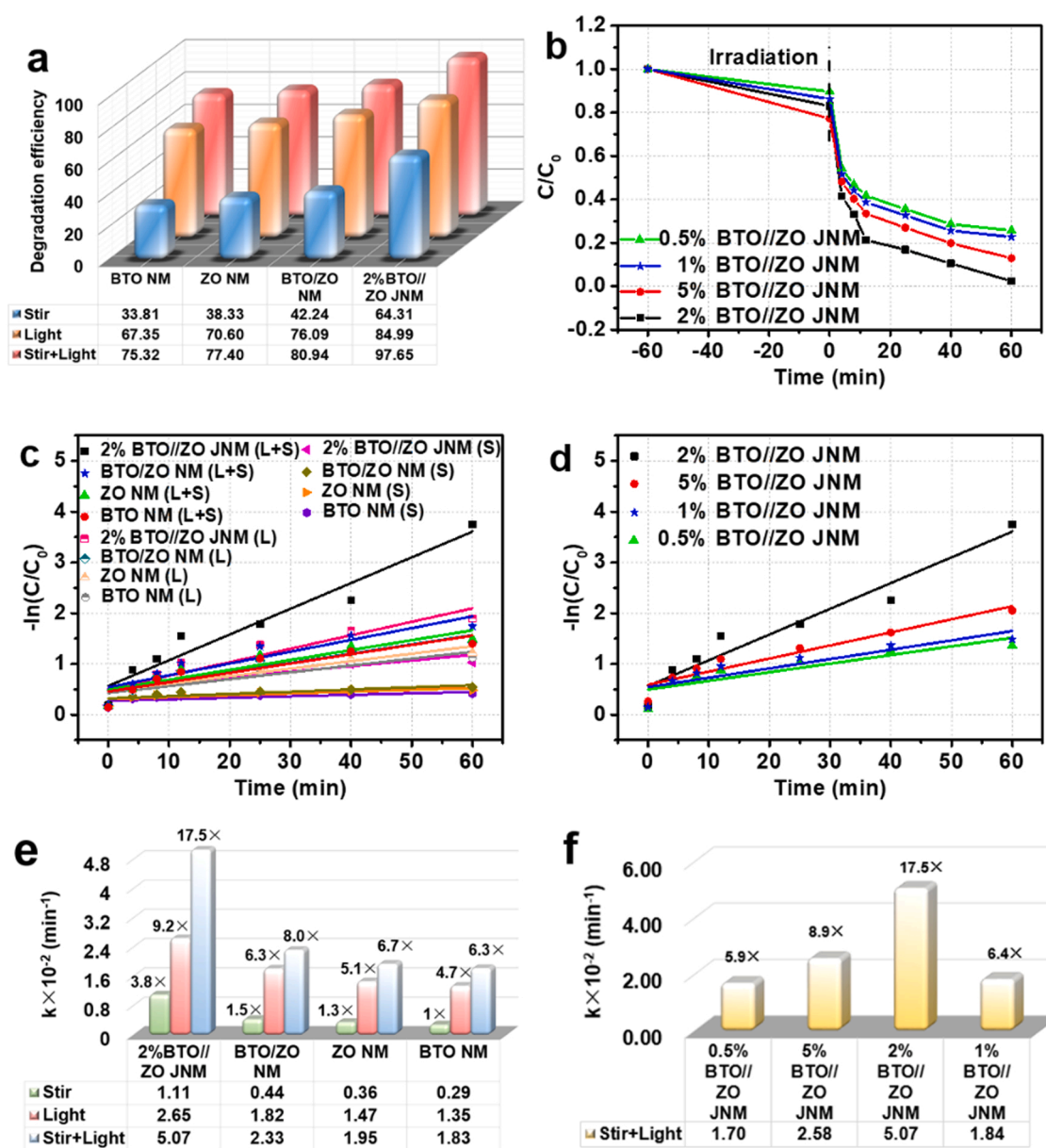


Fig. 4. Piezophotocatalytic degradation efficiencies and their kinetic curves of TC for BTO, ZO, BTO/ZO NM and 2% BTO//ZO JNM under stir, light irradiation and stir+light irradiation (a, c); piezophotocatalytic degradation efficiencies and their kinetic curves of TC for BTO//ZO JNM with different contents of BTO and ZO under stir+light irradiation (b, d); comparison of the first-order rate constant k for TC degradation under different conditions of all membranes (e, f).

due to cross-linking among PVDF, BTO, ZO, PVP, Ni^{2+} , and Cu^{2+} , further showing that $-\text{OH}$ and $-\text{NH}$ are active functional groups in adsorption [55]. The stretching vibrations of $\text{N}-\text{H}$ and $\text{C}-\text{H}$ at 1650 and 2930 cm^{-1} are beneficial to the electrostatic attraction for capturing pollutants [55].

3.2. Adsorption performance

Given that many different kinds of pollutants in practical applications, the Ni^{2+} , Cu^{2+} , MB, CR, TC and BPA were used to evaluate the adsorption capacities and multi-functional catalytic degradation performance of BTO//ZO JNM. The adsorption capacities of 2% BTO//ZO JNM for six different pollutants were studied, as shown in Fig. S6–S10. The results show that the adsorption processes of 2% BTO//ZO JNM for these six pollutants conform to the pseudo-second-order kinetic model, and the adsorption thermodynamic processes conform to the Langmuir model, as shown in Table S1–S2. By comparing the adsorption thermodynamic curves show that the order of the adsorption thermodynamic constant values K_L is $\text{Cu}^{2+} > \text{Ni}^{2+} > \text{TC} > \text{MB} > \text{BPA} > \text{CR}$, indicating that the adsorption order and adsorption capacities of these pollutants are also in this order. In addition, the adsorption capacities of 2% BTO//ZO JNM to inorganic metal ions and organic pollutants in the presence of inorganic and organic pollutants are also considered, respectively. The detailed descriptions are listed in SI (Table S3–S14).

3.3. Piezophotocatalytic performance

Through the dark adsorption experiment analysis, it can be found that there are still a lot of organic contaminants in the solution even if the majority of the metal ions have been adsorbed (Fig. S12 and S13). Therefore, additional treatment piezophotocatalysis technology should be employed.

There are many interferences in multi-pollutants system, so analyzing the piezophotocatalytic performance of 2% BTO//ZO JNM in single pollutant is essential, TC was selected as a pollutant. Firstly, in order to explore the influence of stirring speed on piezophotocatalytic efficiency, we put 2% BTO//ZO JNM under Xe lamp (300 W) and stir (200–1000 rpm) for catalytic reaction. The results are shown in Fig. S14. It can be seen that the degradation efficiency of 2% BTO//ZO JNM on TC increases with the increase of stirring speed, indicating that the stirring speed plays a role in promoting the separation of photogenerated carriers [56]. However, compared with 800 rpm, the degradation efficiency of 2% BTO//ZO JNM is slightly improved (0.876%) under 1000 rpm, the membranes were broken which is not conducive to recovering and maintaining the material structure, thus affecting the later degradation effect. Therefore, we set the stirring speed at 800 rpm. The piezophotocatalytic activity of 2% BTO//ZO JNM in the degradation of TC under light irradiation, stir, and stir+light irradiation was analyzed (Fig. 4) to highlight the excellent performance of 2% BTO//ZO JNM, BTO, ZO and BTO/ZO NM. Within 60 min under light irradiation, 2% BTO//ZO JNM exhibits the TC degradation rate of 84.99%, whereas ZO, BTO and BTO/ZO NM demonstrated TC degradation efficiencies of 70.60%, 67.35%, and 76.09%, respectively (Fig. 4a). These results illustrate that the combination of BTO and ZO can improve photocatalytic degradation efficiency. All the membranes present low TC degradation efficiencies under stir in the dark mainly because the deformation of ZO, BTO and PVDF can create piezoelectric voltages such that the migration of carriers is improved by stir [57], but the piezocatalytic degradation efficiency is not obvious. Under stir+light irradiation, 2% BTO//ZO JNM shows the best catalytic efficiency and completely degrades TC within 60 min (Fig. 4a).

The results in Figs. 4a and 4b verify that the piezophotocatalytic performance of 2% BTO//ZO JNM is obviously superior to that of other membranes. The mechanisms will be discussed in detail later. The reaction rates of all samples are estimated according to the pseudo-first-order kinetic equation, as shown in the following formula:

$$-\ln(C/C_0) = kt \quad (1)$$

where C_0 and C are the TC concentration at initial and t min, respectively. t represents the reaction time, and k is the rate constant. It can be seen that all curves show good linearity, so all the piezophotocatalytic degradation processes accord with first-order reaction, as shown in Figs. 4c and 4d. The piezophotocatalytic degradation rate constants of 2% BTO//ZO JNM are 2.52, 3.04, 3.82, 2.99, 1.97 and 2.75 times than that of BTO/ZO NM, ZO NM, BTO NM, 0.5% BTO//ZO JNM, 5% BTO//ZO JNM and 1% BTO//ZO JNM under stir+light, respectively (Figs. 4e, 4f). Similarly, the rate constants of TC degradation by 2% BTO//ZO JNM are 1.91 and 4.59 times that under light or stir alone, respectively. However, given that piezocatalysis plays a subordinate role in catalysis degradation, photocatalytic performance can be improved with piezoelectric assistance. Additionally, 2% BTO//ZO JNM exhibits the best piezophotocatalytic degradation efficiency than that of other contents of BTO and ZO NPs, as depicted in Figs. 4b, 4d, and 4f. If the BTO and ZO NPs contents in the membrane are inadequate, the amount of Janus heterojunctions to effective degradation of pollutants will also be inadequate. However, the recombination of electrons and holes will reduce catalytic efficiency if the content of the NPs is excessively high. The literature also states that the suitable doping amount for energy harvesting varies from 2 wt% to 10 wt% [58]. Therefore, 2% BTO//ZO JNM is selected as the sample for subsequent degradation experiments. It can be seen that the piezophotocatalytic degradation performance of 2% BTO//ZO JNM is the best under stir+light, it also has better catalytic efficiency than previously reported piezophotocatalysts (Table S15) likely due to its Janus heterostructure.

Considering the practical applications, BPA, CR, MB and TC in Ni^{2+} and Cu^{2+} were used to estimate the piezophotocatalytic degradation efficiency of 2% BTO//ZO JNM (Fig. 5a–h). BPA, CR, MB, and TC in Ni^{2+} and Cu^{2+} cannot be decomposed easily, because metal ions may exert an inhibitory effect on photoelectrons given that metal ions can serve as electrons scavenger [59,60]. The piezophotocatalytic BPA, CR, MB and TC degradation efficiencies of 2% BTO//ZO JNM decrease as the metal concentrations are increased because the residual concentrations increased (see Fig. S15). 2% BTO//ZO JNM exhibits higher piezophotocatalytic degradation efficiency in the Ni^{2+} solution than in the solution with the Cu^{2+} . It can be seen from Fig. S11 that the surfaces of the membranes that degrade organic pollutants in Ni^{2+} solution are only stained with dye, while the surfaces of the membranes that degrade organic pollutants in Cu^{2+} solution are relatively deep because copper green is generated and adhered to the membrane. Cu^{2+} will react with hydroxide in water to generate copper hydroxide, and carbon dioxide will be generated in the process of degrading organic dyes, so it will generate copper green to the membrane to prevent further piezophotocatalytic reactions and thus reduce piezophotocatalytic efficiency [61]. These results proved that 2% BTO//ZO JNM exhibits excellent piezophotocatalytic efficiency and adsorption performance and can be applied in treating multi-pollutants containing Ni^{2+} , Cu^{2+} and organic compounds.

A radical trapping experiment was carried out (Fig. 6a–d) to explore the dominant active radicals during the piezophotocatalytic process over 2% BTO//ZO JNM. FA, IPA, and BQ were used as scavengers for the hole (h^+), hydroxyl ($\bullet\text{OH}$), and superoxide radicals ($\bullet\text{O}_2^-$) [62], respectively. The BPA, CR, MB and TC removal rates in water decrease after the addition of FA, IPA, and BQ, and decrease significantly after adding BQ. These results demonstrate that $\bullet\text{O}_2^-$ dominated the degradation of BPA, CR, MB and TC with h^+ and $\bullet\text{OH}$ playing subordinate roles.

Furthermore, the electron spin resonance (ESR) technique was used to understand the dominant active radicals under various conditions, as shown in Figs. 6e, 6f. For $\bullet\text{OH}$ radicals, there is no obvious characteristic peak under stir, while a significant ESR signal corresponding to $\text{DMPO}-\bullet\text{OH}$ can be found under light and stir+light (Fig. 6e). As shown in Fig. 6f, a very weak peak can be seen under stir, obvious characteristic

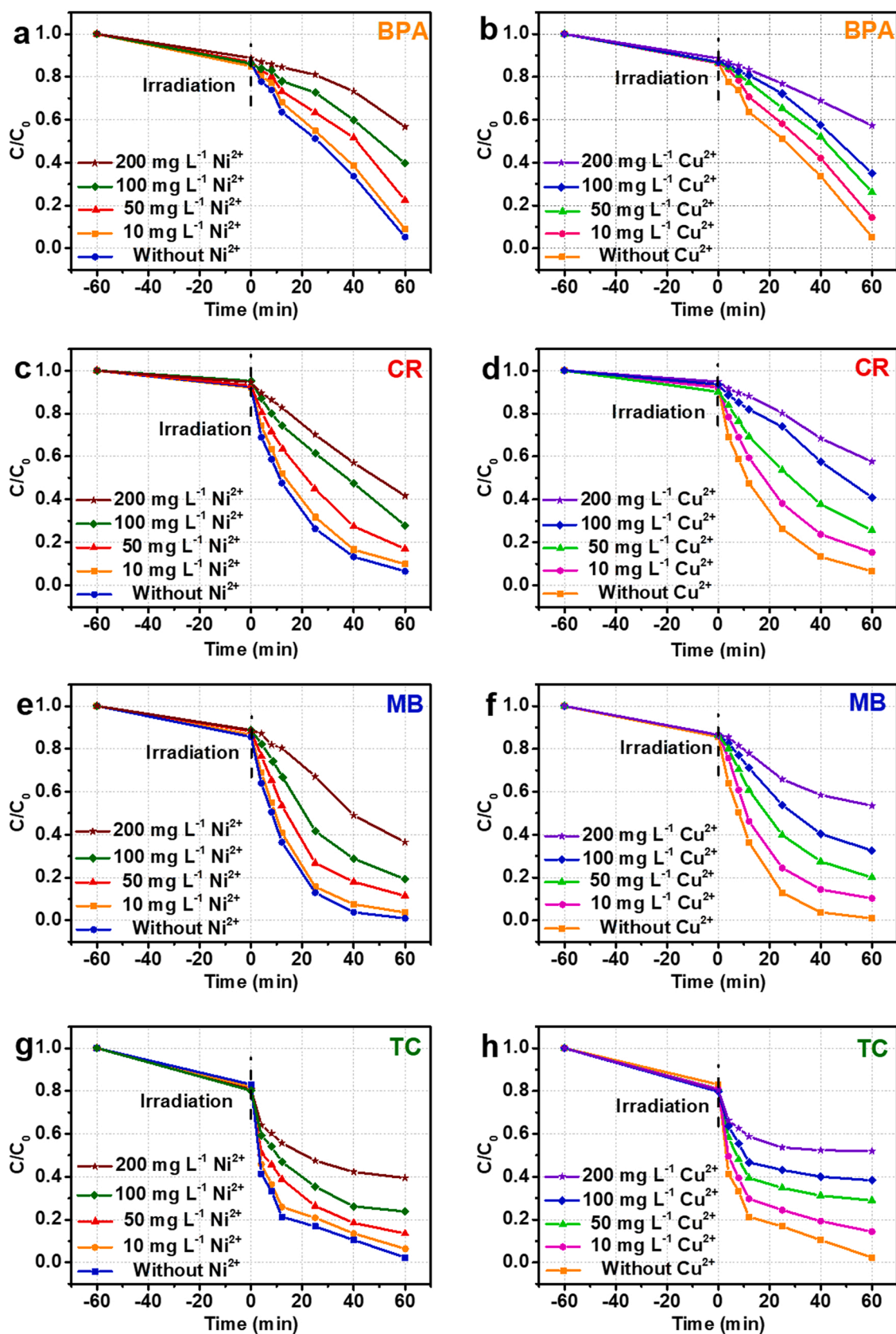


Fig. 5. Removal of BPA, CR, MB and TC in Ni^{2+} (a, c, e, g) and Cu^{2+} (b, d, f, h) solutions with different concentrations.

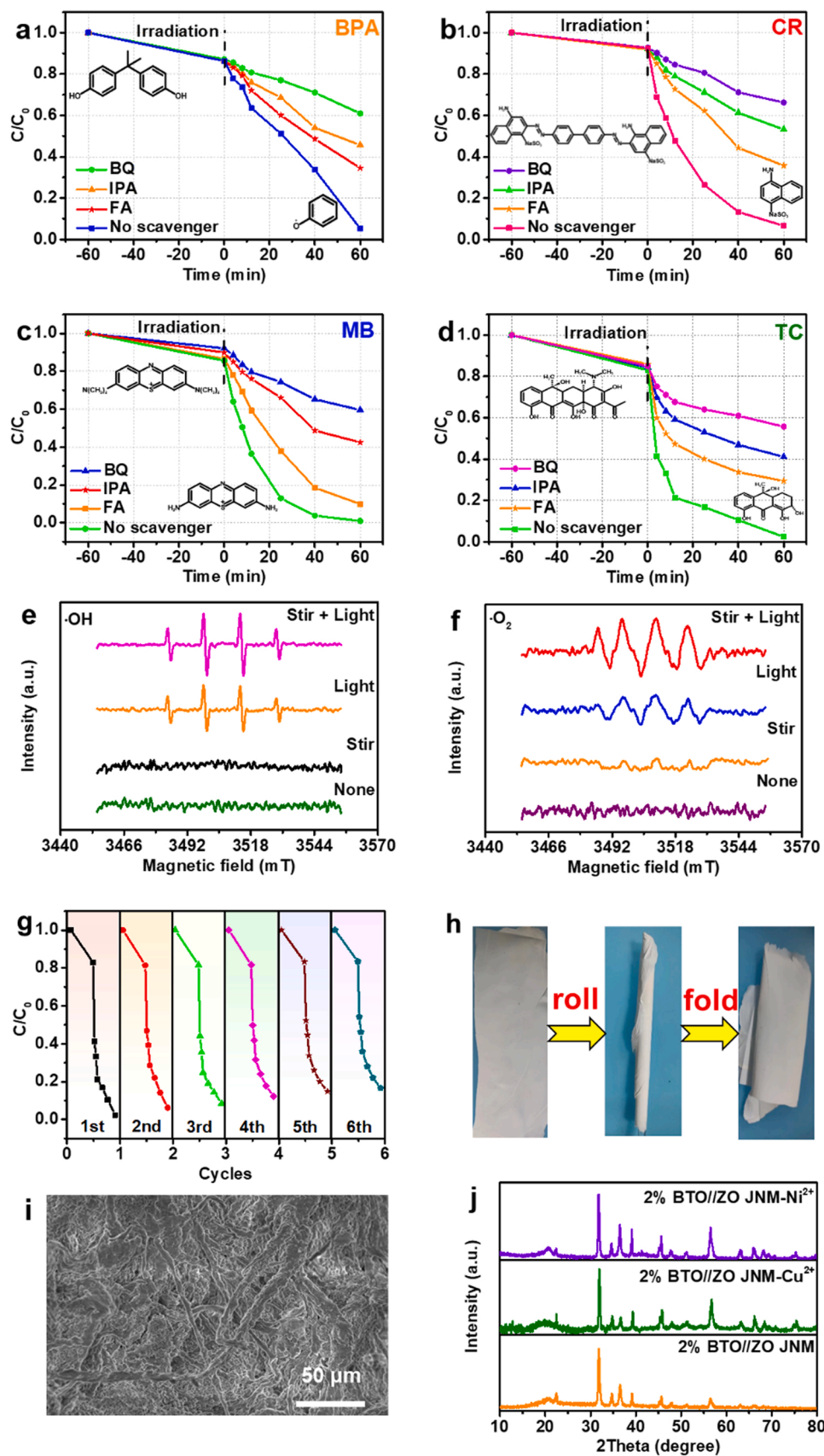


Fig. 6. Piezophotocatalytic oxidation of BPA (a), CR (b), MB (c) and TC (d) degradation with 2% BTO//ZO JNM in the presence of scavengers; ESR signal of $\bullet\text{OH}$ and $\bullet\text{O}_2$ radicals without any irradiation, under stir, light and stir+light irradiation (e, f); the cycling tests on 2% BTO//ZO JNM toward TC in Ni^{2+} solution (g); digital photos of rolled and folding 2% BTO//ZO JNM after six cycles recovery (h); SEM image (i) and XRD patterns (j) of 2% BTO//ZO JNM after six cycles recovery.

peaks relate to ESR signal of $\text{DMPO}-\bullet\text{O}_2^-$ adduct under light and stir+light. It is well acknowledged only the ESR signal intensity of $\bullet\text{O}_2^-$ radicals can be significantly enhanced under stir+light, so the $\bullet\text{O}_2^-$ radicals play a key role in piezophotocatalytic process. Interestingly, it can be found that the improvement of ESR signal intensity produced by stir+light is higher than light which implies that stir is playing an important role in piezophotocatalytic process. It can be concluded that the enhanced degradation efficiency of 2% BTO//ZO JNM can be ascribed to the $\bullet\text{O}_2^-$ radicals enhanced by the stir-induced piezoelectric field [34].

A cycling experiment was carried out to test the stability of the BTO//ZO JNM in the piezophotocatalytic degradation of TC. As depicted in Fig. 6g, piezophotocatalytic degradation efficiency almost remains at 85% after six cycles, indicating that 2% BTO//ZO JNM is relatively stable. Fig. 6h shows that 2% BTO//ZO JNM is flexible. Importantly, after six cycles of recovery, 2% BTO//ZO JNM remains intact, as a result of the low swelling rate of PVDF and the high mechanical strength of PVDF with minimal PVP dissolution. After six times of degradation, the appearance of the nanofibers did not change (Fig. 6i). At the same time, the main characteristic peaks (22.5° , 31.8° , 34.4° , 36.3° , 39.2° , 45.6° , 47.5° , 51.3° , 56.6° , 62.9° , 65.8°) of the samples were almost unchanged from the XRD patterns of the same sample (Fig. 6j). Therefore, JNM can be applied in actual life.

3.4. Mechanism discussion

The mechanisms underlying the treatment of multi-pollutants by 2% BTO//ZO JNM are divided into adsorption and piezophotocatalytic mechanisms as discussed below. XPS was used to investigate the adsorption mechanism of 2% BTO//ZO JNM before and after adsorption. The binding energies of 285.4, 286.4, 288.1, and 291.2 eV in the C 1s spectrum correspond to the C-C, C-O-C, O-C=O [63], -CF bonds [43], respectively, as illustrated in Fig. 7a. At the same time, the N 1s spectra of the membranes have peaks near 399.3 and 399.9 eV representing the -NH- [64] and C-N bonds [51] (Fig. 7b), respectively. The peaks of 528.7, 529.2, 531.2, 528.5, and 529.0 eV in the O 1s spectrum are attributed to the O-H [65], C-O, C=O bonds [66], lattice oxygen, and defect oxygen [67] (Fig. 7d), respectively. In the Ti 2p XPS spectra, the main peak at 459.7 and 465.1 eV meet the $2p_{3/2}$ and $2p_{1/2}$ (Fig. 7c). The peaks of Ba $3d_{5/2}$ and Ba $3d_{3/2}$ that are located at 779.1 and 793.5 eV correspond to BTO (Fig. 7e). The two peaks at 1021.9 and 1045.2 eV (Fig. 7f) originate from the Zn $2p_{3/2}$ and $2p_{1/2}$ in the ZO phase, respectively [48]. The XPS spectra of 2% BTO//ZO JNM after Ni^{2+} and Cu^{2+} adsorption are presented in Figs. 7g and 7h, respectively. The peaks of some functional groups exhibit certain changes after 2% BTO//ZO JNM adsorbed Ni^{2+} (2% BTO//ZO JNM- Ni^{2+}) and Cu^{2+} (2% BTO//ZO JNM- Cu^{2+}). For example, the peaks of C-O (531.5 eV), C=O (532.4 eV), O-H (529.4 eV), lattice oxygen and defect oxygen in the O 1s spectra have moved as exhibited in Fig. 7d. The binding energies of lattice oxygen in 2% BTO//ZO JNM- Ni^{2+} and 2% BTO//ZO JNM- Cu^{2+} are at 529.2, 529.0 eV, respectively. The binding energies at 532.1 and 532.0 eV match defect oxygen of 2% BTO//ZO JNM- Ni^{2+} , and BTO//ZO JNM- Cu^{2+} , respectively. They may be due to the fact that the electron cloud density around the oxygen atom decreases after 2% BTO//ZO JNM combined with Ni^{2+} [50] and Cu^{2+} [65]. The C 1s peak shows no remarkable change in position but demonstrates a change in the peak area. In addition, new peaks located at 397.5 eV (Ni-N) [64] and 406.5 eV (Cu-N) [68] are found in the N 1s spectra. The above analyses show that the hydroxyl and amino groups on 2% BTO//ZO JNM can adsorb Ni^{2+} and Cu^{2+} . Furthermore, the Ni 2p and Cu 2p spectra of 2% BTO//ZO JNM after adsorption are recorded. The binding energies in the Ni 2p spectrum are ascribed to the Ni-O (860.8 eV) and Ni-N (854.3 eV) bonds [69]. Similarly, the Cu 2p spectrum is divided into two peaks that corresponded to the Cu-N (936.3 eV) and Cu-O (933.4 eV) bonds [68]. These results further prove that Ni^{2+} and Cu^{2+} have been adsorbed onto 2% BTO//ZO JNM.

In general, the connected two semiconductors will form heterojunction [70]. XPS was used to characterize this phenomenon, as shown in Fig. S16. As can be observed, Zn, Ba, O, Ti, C, and F make up 2% BTO//ZO JNM. PVDF is composed of O, N, C and F. Zn, Ba, O, and Ti come from ZO and BTO. Interestingly, the heterojunction is formed in 2% BTO//ZO JNM, which is indicated by the binding energy of 2% BTO//ZO JNM being between that of ZO and BTO [48]. In the BTO NM spectrum, the binding energies at 464.1 eV and 458.4 eV match Ti $2p_{1/2}$ and Ti $2p_{3/2}$, respectively (Fig. S16a) [48]. The 2% BTO//ZO JNM spectrum has peak values of 464.7 eV and 459.7 eV, respectively. The binding energy could transfer to the high energy field as a result of the built-in electric field in the 2% BTO//ZO JNM [67]. The high-resolution Ba 3d spectrum of 2% BTO//ZO JNM (Fig. S16b) reveals that the Ba $3d_{3/2}$ and Ba $3d_{5/2}$ peaks shift to high energies of 793.5 eV and 779.1 eV, respectively [48]. The Zn 2p signal exhibits the same trend at the same time (Fig. S16c). The binding energies in ZO NM at 1043.7 eV and 1021.5 eV which correspond to Zn $2p_{1/2}$ and Zn $2p_{3/2}$ shift to 1045.2 eV and 1021.9 eV, respectively [67]. The peaks in the O 1s spectrum match adsorbed, defect, and lattice oxygen from left to right, respectively (Fig. S16d) [67]. The binding energies at 528.3 eV, 528.9 eV, and 528.5 eV match the lattice oxygen of ZO, BTO, and 2% BTO//ZO JNM, respectively [67]. These findings suggest that the 2% BTO//ZO JNM contains heterojunction.

The UV-Vis absorption spectra of BTO and ZO NM are depicted in Fig. 8a. The band gap of BTO ZO NM are 2.90 eV and 2.98 eV, respectively [4,33,48]. Given that these materials have bandgaps of less than 3.10 eV, they can absorb light with wavelength below 400 nm. The Mott-Schottky plots of BTO and ZO NM were acquired at different frequencies to verify the potential of the conduction band (E_{CB}) and valence band (E_{VB}), as shown in Fig. S17. The E_{CB} of BTO and ZO NM are -0.52 V and -0.68 V, respectively. The slopes of them are positive, implying that BTO and ZO NM are n-type semiconductors; therefore, the BTO//ZO JNM is an n-n type heterostructured material [48]. The PL test is conducted to investigate the capability for electrons and holes separation and transport (Fig. 8b). BTO/ZO NM exhibits lower PL peak intensity than BTO, ZO NM because it contains Janus heterojunctions. Among all membranes, 2% BTO//ZO JNM has the lowest PL intensity because of the formation of a large amount of Janus heterojunctions formed at the interface of the Janus nanofibers in 2% BTO//ZO JNM. This result suggests that 2% BTO//ZO JNM exhibits prolonged charge carrier lifetime that will cause higher piezophotocatalytic activity [71]. The photocurrent-time response test reveals that the photocurrents of all the membranes increase under light and are stable because of the charge recombination. 2% BTO//ZO JNM possesses strong photoelectric conversion efficiency because of its Janus heterojunctions (Fig. 8c). EIS tests are performed to study the electron and hole transport properties of the membranes as presented in Fig. 8d and S18. 2% BTO//ZO JNM has the lowest radius, followed by BTO/ZO NM, 5% BTO//ZO JNM, 1% BTO//ZO JNM, BTO, and ZO NM. These results suggest that 2% BTO//ZO JNM has the highest electron-hole pairs separation efficiency. In other words, the radius decreases after the formation of BTO//ZO Janus heterojunctions. If the contents of ZO and BTO are increased beyond the optimal value (5% BTO//ZO JNM), the resistance will likely increase again because the excess amount of ZO and BTO NPs will recombine, which will accelerate charges to reunite in BTO//ZO JNM. These above results suggest that Janus heterojunctions can enhance the transport rate of charges at the interface of the Janus nanofibers. Therefore, 2% BTO//ZO JNM has the best piezophotocatalytic property.

The relationship between piezoelectric potential and the photocatalytic process was determined through COMSOL computational simulation. In fact, the piezoelectric potential elicited by stir-induced shearing force has been confirmed in $\text{Pb}(\text{Zr}, \text{Ti})\text{O}_3/\text{TiO}_2$, ZO nanorods/PVDF films, BTO@Au NPs hybrid materials [10,72,73]. The pressure was exerted under stir. This pressure plays an important role in the formation of piezoelectric field in the 2% BTO//ZO JNM. On the other hand, stir can generate bubbles which cause local pressure. The pressure

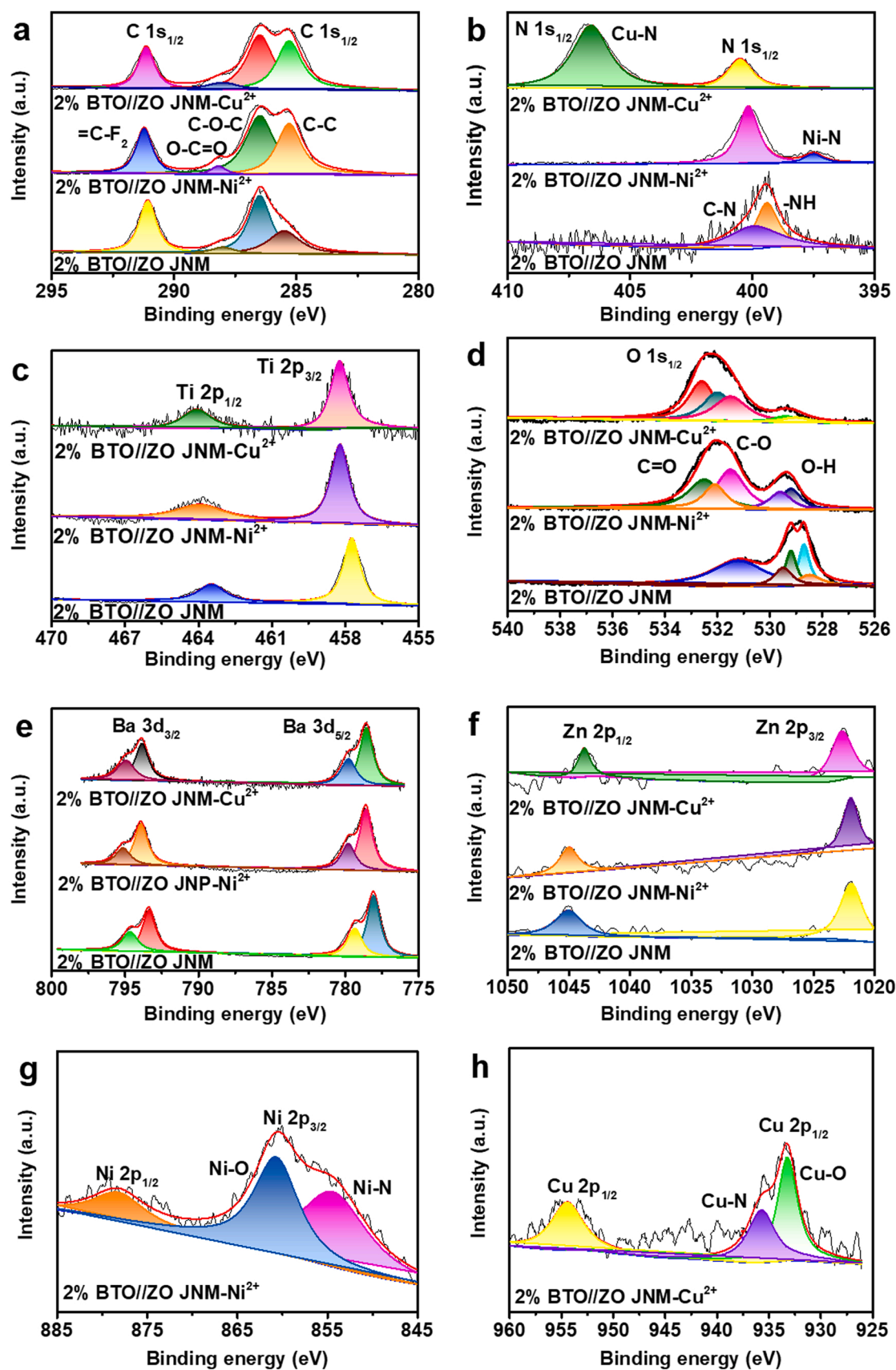


Fig. 7. C 1s (a), N 1s (b), Ti 2p (c), O 1s (d), Ba 3d (e), Zn 2p (g), Ni 2p (g) and Cu 2p (h) spectra of 2% BTO//ZO JNM.

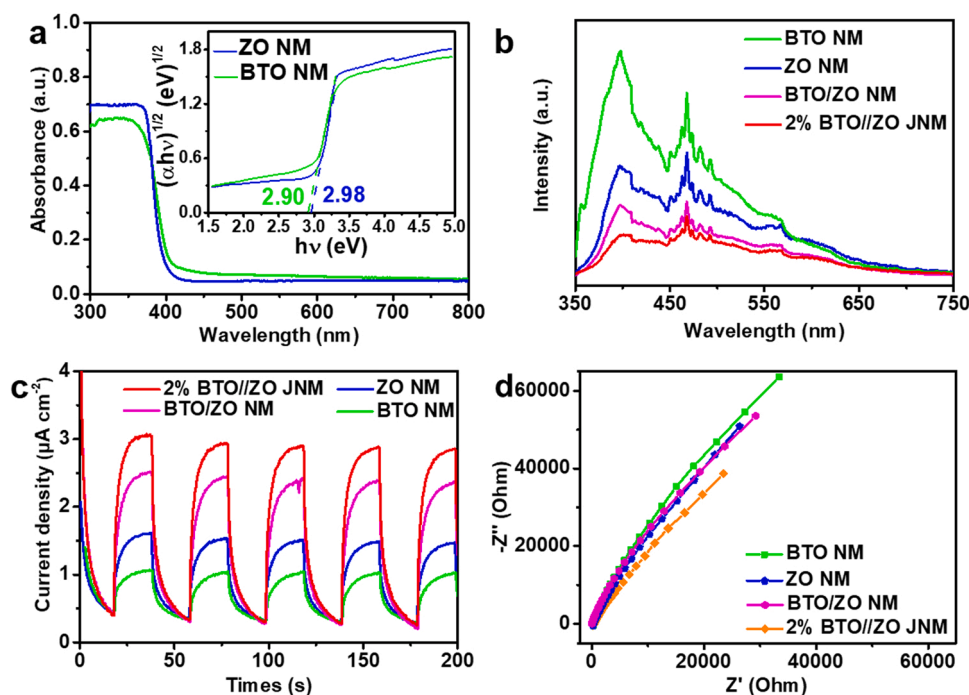


Fig. 8. UV-Vis absorption spectra of BTO and ZO NM (a); plots of $(\alpha h\nu)^{1/2}$ versus $h\nu$ of BTO and ZO NM (Inset); PL spectra of BTO, ZO, BTO/ZO NM and 2% BTO//ZO JNM (b); photocurrent-time response curves of BTO, ZO, BTO/ZO NM and 2% BTO//ZO JNM (c); EIS Nyquist plots of BTO, ZO, BTO/ZO NM and 2% BTO//ZO JNM (d).

of water can exert strain on the BTO, ZO NPs PVDF which can transport to 2% BTO//ZO JNM. A piezoelectric field is created on the nanofiber membrane when 2% BTO//ZO JNM is crossing the negative and positive regions of the strain [14]. Given that a previous report [58] has shown that electric field intensity is highest when the mixing amount is 2%, the effect of optimal contents of BTO and ZO NPs on the piezoelectric potential difference will not be discussed in the following section. In addition, given that the force on the membrane is complex, the model is simplified to simulate single nanofiber in the membrane. The strain and piezoelectric potential on the surface of BTO, ZO, BTO/ZO nanofiber and 2% BTO//ZO Janus nanofiber differ under strain and correspond to those on authentic simulation models as displayed in Fig. 9. The piezoelectric potential differences of BTO nanofiber is 168.50 mV under external pressure (Fig. 9a). This result verifies that BTO nanofiber can be polarized easily. The ZO nanofiber causes a piezoelectric potential difference of 83.00 mV (Fig. 9b) which is lower than that caused by BTO nanofiber. This result indicates that the piezophotocatalytic capability of BTO nanofiber is higher than that of ZO nanofibers. In particular, the piezoelectric potential differences of BTO/ZO nanofiber and 2% BTO//ZO Janus nanofiber are 256.20 mV and 338.60 mV (Figs. 9c and 9d), respectively, which are considerably higher than those of BTO and ZO nanofiber, indicating that BTO//ZO heterostructures enhance macroscopic polarization. Therefore, sufficient mechanochemical potential can promote catalytic oxidations reaction. The slightly higher piezoelectric potential difference of 2% BTO//ZO Janus nanofiber indicates the superiority of Janus nanofiber. Although BTO/ZO nanofiber and BTO//ZO Janus nanofiber contain Janus NPs, the excess Janus NPs easily aggregate and accumulate centrosymmetric localization of the plasmonic near-fields in the BTO/ZO nanofiber [74], and there are many Janus NPs immerse in the BTO/ZO nanofiber. As for BTO//ZO Janus nanofibers, Janus NPs that appear at the interface of BTO//ZO Janus nanofibers will not create centrosymmetric localization of the plasmonic near-fields.

The intermediates and final products in the degradation process were determined by high performance liquid chromatography-mass spectrometry (HPLC-MS). According to the results and papers, the possible

degradation pathways of MB, CR, TC and BPA are assumed, as shown in Fig. S19–S30. The analysis results of these four pollutants are listed in SI. Through LCMS test, it shows that 2% BTO//ZO JNM exhibits excellent piezophotodegradation performance.

The mechanisms of charge transfer in 2% BTO//ZO JNM are proposed to understand the piezophotocatalytic effect in pollutants degradation. As shown in Fig. 10, the stir energy and the pressure released by cavitation bubbles will cause the deformation of 2% BTO//ZO JNM at different degrees. In the process of piezophotocatalysis, BTO and ZO nanofibers can bend randomly, thus generating positive and negative piezoelectric potentials. The interface electric field is generated between BTO, ZO and PVDF, which accelerates the migration of photogenerated carriers. Even though the heterojunction can separate some photogenerated carriers under light, this internal electric field is static and easily saturated by the external shielding effect, thus the photogenerated electron-hole pairs are reduced, which will also cause the low photocatalytic efficiency [67] (Fig. 10a). When stir is added to the system, the introduction of piezoelectric field breaks the shielding effect of piezoelectric enhancement system. However, the shielding effect still exists when the generation time of piezoelectric potential is shorter than the recombination time of photogenerated electron-hole. Therefore, the reaction rates of piezophotocatalysis are not significantly improved of ZO, BTO and BTO/ZO NM. For piezoelectric enhancement photocatalyst systems, different deformation directions or degrees of BTO, ZO and PVDF may lead to different initial times of piezoelectric potential generation of their respective materials. Therefore, the asynchronous changes of BTO, ZO and PVDF piezoelectric fields will alternately destroy the shielding effect and shorten the degradation time even if the shielding effect exists. It also explains why the piezophotocatalytic reaction rate of 2% BTO//ZO JNM is higher than that of other membranes. In addition, one-dimensional BTO nanofibers and ZO nanofibers are easily deformed to generate piezoelectric fields. Stir stimulus may generate eddy currents to attack these nanofibers. The deformation directly affects the piezoelectric potential, so stir treatment is particularly important. Even if the energy in the stirring liquid medium is reduced due to heat exchange, the continuous input of stir ensures the

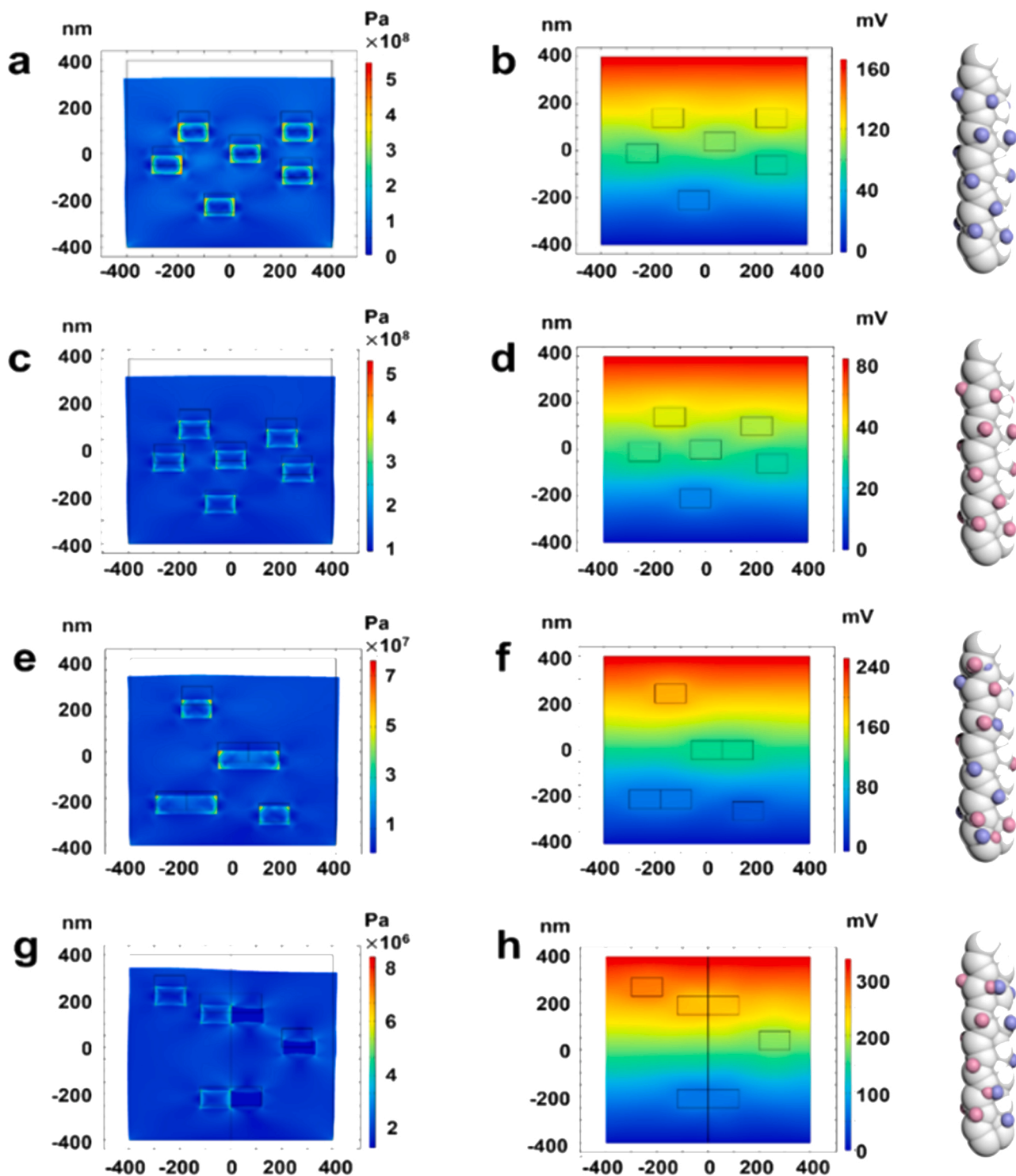


Fig. 9. Strain and electric field distribution of BTO nanofiber (a, b), ZO nanofiber (c, d), BTO/ZO nanofiber (e, f) and 2% BTO//ZO Janus nanofiber (g, h).

continuous deformation of the membrane, and the formed piezoelectric field can continuously separate the photogenerated carriers and participate in the redox reaction. Most importantly, the Janus structure can avoid the centrosymmetric localization of the plasmonic near-fields effect which can maximize the piezophotocatalytic effect [74].

Fig. 10 shows the state of the electrons and holes in 2% BTO//ZO JNM under light and stir+light irradiation. As depicted in Fig. 10a, there is no piezoelectric effect in PVDF under light, and the electrons and charges in it do not move in PVDF, so the transport direction of electrons is similar to whether BTO or ZO is in contact with PVDF. The holes on

the VB of ZO are transported to the VB of BTO, and the O_2/H_2O potential is lower than the E_{VB} of BTO, so OH^- and H_2O can be oxidized into $\bullet OH$. While the electrons are transported from the CB of BTO to the CB of ZO, the electrons on the CB can reduce the O_2 into $\bullet O_2^-$ because the O_2/O_2^- potential is higher than that of the E_{CB} of ZO. In addition, ZO can provide higher electron mobility than BTO, such that the ZO surface can generate additional $\bullet O_2^-$ [75]. These reactive radicals can degrade pollutants. This phenomenon prevents the recombination of electrons and holes in BTO and ZO. Therefore photocatalytic efficiency is enhanced compared with BTO and ZO under light irradiation (Fig. 4). Bound

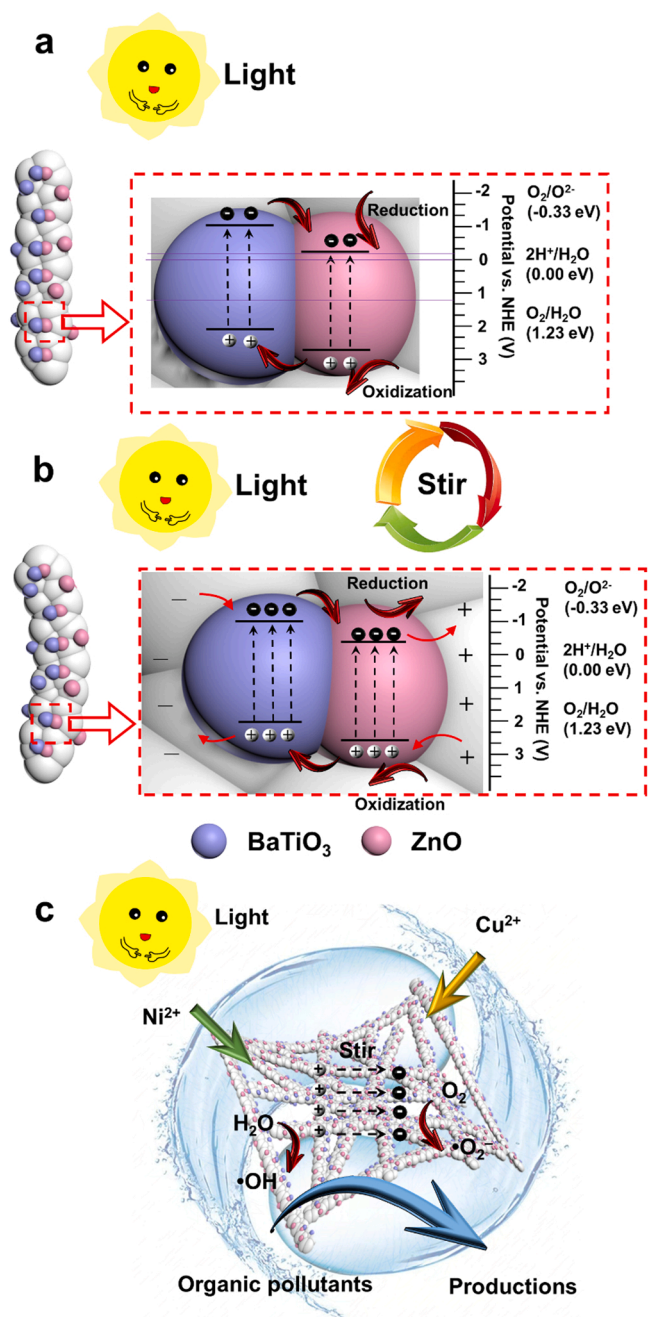


Fig. 10. Piezophotocatalytic mechanisms of 2% BTO//ZO JNM under light irradiation (a) and stir+light irradiation (b); the schematic of pollutants degradation by 2% BTO//ZO JNM (c).

surface charges can also be formed through the piezoelectric polarization of 2% BTO//ZO JNM under stir, resulting in the formation of a built-in electric field in 2% BTO//ZO JNM (Fig. 10b). The electrons and holes are moved by built-in electric fields toward inverse directions. In addition, built-in electric fields can be improved by introducing PVDF because the piezoelectrical property PVDF can transport carriers under stir. The forming built-in electric fields provide electrons to the CB of BTO, which increases the number of electrons from BTO to ZO. While the forming holes in PVDF can also accept the holes from ZO to BTO which significantly inhibits the recombination of electrons and holes in BTO and ZO [57]. The additional separation electrons and holes can also react with O_2 and H_2O to generate free radicals to enhance degradation efficiency (Fig. 10c). Therefore, the carriers separation efficiency under

stir+light is higher than that of those under light irradiation only. Furthermore, given the large surface area of the bamboo-like 2% BTO//ZO JNM (BET test), the excessive number of BTO and ZO NPs can be exposed such that the transport paths of charge carriers are shortened. The reactions of the piezophotodegradation pollutants are as follows:



4. Conclusion

In summary, the highly flexible BTO//ZO JNM was developed through side-by-side electrospinning and proven to be a multifunctional catalyst for the simultaneous adsorption of heavy metals and removal of organic pollutants under light irradiation and stir. The piezophotocatalysis efficiencies of 2% BTO//ZO JNM for simultaneous removal of TC, CR, MB, and BPA achieved 93.65%, 90.12%, 96.33% and 91.05% in Ni^{2+} solution within 60 min, respectively. And the adsorption capacity of BTO//ZO JNM for Ni^{2+} and Cu^{2+} are also highly to 462.2 and 477.4 mg g^{-1} , respectively. The excellent adsorption and piezophotocatalysis performance of 2% BTO//ZO JNM can be attributed to the addition of the piezoelectric components of BTO and ZO NPs. Compared with uniaxial blend nanofibrous membrane, 2% BTO//ZO JNM exhibited excellent properties owing to unique nanofibrous Janus heterostructures, which can avoid the effect of centrosymmetric localization of the plasmonic near-fields, built the internal electric field of the n-n heterojunction to achieve rapid and complete degradation of organic pollutions, and promote the charge transfer and prevent the recombination of electron-hole pairs under stir and light activation. This work provides a unique durable and flexible membrane to adsorb Ni^{2+} , Cu^{2+} and the piezophotocatalytic degradation multi-pollutants. It also provides deep insights into the piezophotocatalytic mechanism of Janus heterostructured nanofibers. Future works will focus on the effective utilization of environmental vibrations, stir, and/or light irradiation to drive electron-hole separation and transfer in piezophotocatalytic membranes in pollutant and gas treatment and energy regeneration.

CRediT authorship contribution statement

He Lv: Investigation, Data curation, Writing – original draft, **Yanan Liu:** Validation, Investigation, Data curation, Conceptualization, Supervision, Methodology, Writing – review & editing, **Ping Zhao:** Formal analysis, Investigation, **Yubin Bai:** Formal analysis, Investigation, **Wenxin Cui:** Formal analysis, Investigation, **Shuling Shen:** Formal analysis, Investigation, **Yang Liu:** Formal analysis, Investigation, **Zheng Wang:** Investigation, Conceptualization, Methodology, **Deng-Guang Yu:** Conceptualization, Supervision, Methodology, Writing – review & editing, Funding acquisition.

Declaration of Competing Interest

The authors declare that they have no known competing financial interests or personal relationships that could have appeared to influence the work reported in this paper.

Data availability

No data was used for the research described in the article.

Acknowledgements

The following financial supports are appreciated: The Natural Science Foundation of Shanghai (No.20ZR1439000).

Appendix A. Supporting information

Supplementary data associated with this article can be found in the online version at doi:10.1016/j.apcatb.2023.122623.

References

- J. Jin, J.P. Kim, S. Wan, K.H. Kim, Y. Choi, P. Li, J. Kang, Z. Ma, J.H. Lee, O. Kwon, D.W. Kim, J.H. Park, Hierarchical pore enhanced adsorption and photocatalytic performance of graphene oxide/Ti-based metal-organic framework hybrid for toluene removal, *Appl. Catal. B-Environ.* 317 (2022), 121751.
- A. Giwa, A. Dindi, J. Kujawa, Membrane bioreactors and electrochemical processes for treatment of wastewaters containing heavy metal ions, organics, micropollutants and dyes: Recent developments, *J. Hazard. Mater.* 370 (2019) 172–195.
- L. Zhou, S. Dai, S. Xu, Y. She, Y. Li, S. Leveneur, Y. Qin, Piezoelectric effect synergistically enhances the performance of $\text{Ti}_{32}\text{-oxo-cluster/BaTiO}_3/\text{CuS}$ p-n heterojunction photocatalytic degradation of pollutants, *Appl. Catal. B-Environ.* 291 (2021), 120019.
- F. Sun, H. Qi, Y. Xie, Q. Ma, W. He, D. Xu, G. Wang, W. Yu, T. Wang, X. Dong, Flexible self-supporting bifunctional $[\text{TiO}_2/\text{C}]/[\text{Bi}_2\text{WO}_6/\text{C}]$ carbon-based Janus nanofiber heterojunction photocatalysts for efficient hydrogen evolution and degradation of organic pollutant, *J. Alloy. Compd.* 830 (2020), 154673.
- Y.N. Ding, L. Xie, W. Zhou, F. Sun, J.H. Gao, C.W. Yang, G.B. Zhao, Y.K. Qin, J. Ma, Pulsed electrocatalysis enables the stabilization and activation of carbon-based catalysts towards H_2O_2 production, *Appl. Catal. B-Environ.* 316 (2022), 121688.
- X.L. Dong, Z.M. Wang, A. Berbille, X. Zhao, W. Tang, Z.L. Wang, Investigations on the contact-electro-catalysis under various ultrasonic conditions and using different electrification particles, *Nano Energy* 99 (2022), 107346.
- Z.M. Wang, A. Berbille, Y.W. Feng, S. Li, L.P. Zhu, W. Tang, Z.L. Wang, Contact-electro-catalysis for the degradation of organic pollutants using pristine dielectric powders, *Nat. Commun.* 13 (2022) 130.
- S. Xu, W. Qian, D. Zhang, X. Zhao, X. Zhang, C. Li, C.R. Bowen, Y. Yang, A coupled photo-piezoelectric effect in a BST-PDMS porous foam for enhanced dye wastewater degradation, *Nano Energy* 77 (2020), 105305.
- M. Ji, J.H. Kim, C.-H. Ryu, Y.-I. Lee, Synthesis of self-modified black BaTiO_{3-x} nanoparticles and effect of oxygen vacancy for the expansion of piezocatalytic application, *Nano Energy* 95 (2022), 106993.
- Y. Feng, H. Li, L. Ling, S. Yan, D. Pan, H. Ge, H. Li, Z. Bian, Enhanced photocatalytic degradation performance by fluid-induced piezoelectric field, *Environ. Sci. Technol.* 52 (2018) 7842–7848.
- C. Zhang, W. Fei, H. Wang, N. Li, D. Chen, Q. Xu, H. Li, J. He, J. Lu, p-n heterojunction of BiOI/ZnO nanorod arrays for piezo-photocatalytic degradation of bisphenol A in water, *J. Hazard. Mater.* 399 (2020), 123109.
- H. You, X. Ma, Z. Wu, L. Fei, X. Chen, J. Yang, Y. Liu, Y. Jia, H. Li, F. Wang, H. Huang, Piezoelectrically/pyroelectrically-driven vibration/cold-hot energy harvesting for mechano-/pyro- bi-catalytic dye decomposition of NaNbO_3 nanofibers, *Nano Energy* 52 (2018) 351–359.
- P. Wang, X. Li, S. Fan, X. Chen, M. Qin, D. Long, M.O. Tade, S. Liu, Impact of oxygen vacancy occupancy on piezo-catalytic activity of BaTiO_3 nanobelt, *Appl. Catal. B-Environ.* 279 (2020), 119340.
- A. Durairaj, S. Ramasundaram, T. Sakthivel, S. Ramanathan, A. Rahaman, B. Kim, S. Vasanthkumar, Air bubbles induced piezophotocatalytic degradation of organic pollutants using nanofibrous poly(vinylidene fluoride)-titanium dioxide hybrid, *Appl. Surf. Sci.* 493 (2019) 1268–1277.
- X. Zhou, F. Yan, S. Wu, B. Shen, H. Zeng, J. Zhai, Remarkable piezophoto coupling catalysis behavior of $\text{BiOX}/\text{BaTiO}_3$ ($X = \text{Cl}, \text{Br}, \text{Cl}_{0.166}\text{Br}_{0.834}$) piezoelectric composites, *Small* 16 (2020) 2001573.
- D. Yu, Z. Liu, J. Zhang, S. Li, Z. Zhao, L. Zhu, W. Liu, Y. Lin, H. Liu, Z. Zhang, Enhanced catalytic performance by multi-field coupling in KNbO_3 nanostructures: Piezo-photocatalytic and ferro-photoelectrochemical effects, *Nano Energy* 58 (2019) 695–705.
- S. Singh, N. Khare, Coupling of piezoelectric, semiconducting and photoexcitation properties in NaNbO_3 nanostructures for controlling electrical transport: Realizing an efficient piezo-photoanode and piezo-photocatalyst, *Nano Energy* 38 (2017) 335–341.
- J.M. Wu, W.E. Chang, Y.T. Chang, C. Chang, Piezo-catalytic effect on the enhancement of the ultra-high degradation activity in the dark by single- and few-layers MoS_2 nanoflowers, *Adv. Mater.* 28 (2016) 3718–3725.
- Q. Shi, M. Zhang, Z. Zhang, Y. Li, Y. Qu, Z. Liu, J. Yang, M. Xie, W. Han, Energy and separation optimization of photogenerated charge in BiVO_4 quantum dots by piezo-potential for efficient gaseous pollutant degradation, *Nano Energy* 69 (2020), 104448.
- M.-K. Lo, S.-Y. Lee, K.-S. Chang, Study of ZnSnO_3 -nanowire piezophotocatalyst using two-step hydrothermal synthesis, *J. Phys. Chem. C* 119 (2015) 5218–5224.
- Z. Kang, K. Ke, E. Lin, N. Qin, J. Wu, R. Huang, D. Bao, Piezoelectric polarization modulated novel $\text{Bi}_2\text{WO}_6/\text{g-C}_3\text{N}_4/\text{ZnO}$ Z-scheme heterojunctions with $\text{g-C}_3\text{N}_4$ intermediate layer for efficient piezo-photocatalytic decomposition of harmful organic pollutants, *J. Colloid Interf. Sci.* 607 (2022) 1589–1602.
- S. Tu, H. Huang, T. Zhang, Y. Zhang, Controllable synthesis of multi-responsive ferroelectric layered perovskite-like $\text{Bi}_4\text{Ti}_3\text{O}_{12}$: photocatalysis and piezoelectric-catalysis and mechanism insight, *Appl. Catal. B-Environ.* 219 (2017) 550–562.
- H. Huang, S. Tu, X. Du, Y. Zhang, Ferroelectric spontaneous polarization steering charge carriers migration for promoting photocatalysis and molecular oxygen activation, *J. Colloid Interf. Sci.* 509 (2018) 113–122.
- J. Hu, Y. Chen, Y. Zhou, L. Zeng, Y. Huang, S. Lan, M. Zhu, Piezo-enhanced charge carrier separation over plasmonic Au-BiOBr for piezo-photocatalytic carbamazepine removal, *Appl. Catal. B-Environ.* 311 (2022), 121369.
- Y. Wei, Y. Zhang, W. Geng, H. Su, M. Long, Efficient bifunctional piezocatalysis of Au/BiVO_4 for simultaneous removal of 4-chlorophenol and Cr(VI) in water, *Appl. Catal. B-Environ.* 259 (2019), 118084.
- S. Lan, J. Feng, Y. Xiong, S. Tian, S. Liu, L. Kong, Performance and mechanism of piezo-catalytic degradation of 4-chlorophenol: finding of effective piezo-dechlorination, *Environ. Sci. Technol.* 51 (2017) 6560–6569.
- X. Xu, Z. Wu, L. Xiao, Y. Jia, J. Ma, F. Wang, L. Wang, M. Wang, H. Huang, Strong piezo-electro-chemical effect of piezoelectric BaTiO_3 nanofibers for vibration-catalysis, *J. Alloy. Compd.* 762 (2018) 915–921.
- J. Yuan, X. Huang, L. Zhang, F. Gao, R. Lei, C. Jiang, W. Feng, P. Liu, Tuning piezoelectric field for optimizing the coupling effect of piezo-photocatalysis, *Appl. Catal. B-Environ.* 278 (2020), 119291.
- Z. Yao, H. Sun, S. Xiao, Y. Hu, X. Liu, Y. Zhang, Synergetic piezo-photocatalytic effect in a $\text{Bi}_2\text{MoO}_6/\text{BiOBr}$ composite for decomposing organic pollutants, *Appl. Surf. Sci.* 560 (2021), 150037.
- Y. Li, R. Li, Y. Zhai, Y. Huang, S. Lee, J. Cao, Improved photocatalytic activity of $\text{BaTiO}_3/\text{La}_2\text{Ti}_2\text{O}_7$ heterojunction composites via piezoelectric-enhanced charge transfer, *Appl. Surf. Sci.* 570 (2021), 151146.
- Y. Bai, J. Zhao, Y. Li, Z. Lv, K. Lu, Preparation and photocatalytic performance of $\text{TiO}_2/\text{PbTiO}_3$ fiber composite enhanced by external force induced piezoelectric field, *J. Am. Ceram. Soc.* 102 (2019) 5415–5423.
- U. Farooq, P. Chaudhary, P.P. Ingole, A. Kalam, T. Ahmad, Development of cuboidal $\text{KNbO}_3/\alpha\text{-Fe}_2\text{O}_3$ hybrid nanostructures for improved photocatalytic and photoelectrocatalytic applications, *ACS Omega* 5 (2020) 20491–20505.
- C. Zhang, N. Li, D. Chen, Q. Xu, H. Li, J. He, J. Lu, The ultrasonic-induced-piezoelectric enhanced photocatalytic performance of ZnO/CdS nanofibers for degradation of bisphenol A, *J. Alloy. Compd.* 885 (2021), 160987.
- Y. Fu, Z. Ren, J. Wu, Y. Li, W. Liu, P. Li, L. Xing, J. Ma, H. Wang, X. Xue, Direct Z-scheme heterojunction of ZnO/MoS_2 nanoarrays realized by flowing-induced piezoelectric field for enhanced sunlight photocatalytic performances, *Appl. Catal. B-Environ.* 285 (2021), 119785.
- Q. Liu, F. Zhan, H. Luo, D. Zhai, Z. Xiao, Q. Sun, Q. Yi, Y. Yang, D. Zhang, Mechanism of interface engineering for ultrahigh piezo-photoelectric catalytic coupling effect of $\text{BaTiO}_3/\text{TiO}_2$ microflowers, *Appl. Catal. B-Environ.* 318 (2022), 121817.
- H. Lv, M. Zhang, P. Wang, X. Xu, Y. Liu, D.-G. Yu, Ingenious construction of $\text{Ni}(\text{DMG})_2/\text{TiO}_2$ -decorated porous nanofibers for the highly efficient photodegradation of pollutants in water, *Colloid Surf. A* 650 (2022), 129561.
- S. Pradhan, D. Ghosh, S. Chen, Janus nanostructures based on Au-TiO_2 heterodimers and their photocatalytic activity in the oxidation of methanol, *ACS Appl. Mater. Inter.* 1 (2009) 2060–2065.
- J. Yang, K. Wang, D.-G. Yu, Y. Yang, S.W.A. Bligh, G.R. Williams, Electrospun Janus nanofibers loaded with a drug and inorganic nanoparticles as an effective antibacterial wound dressing, *Mat. Sci. Eng. C -Mater.* 111 (2020), 110805.
- H. Xu, F. Zhang, M. Wang, H. Lv, D.-G. Yu, X. Liu, H. Shen, Electrospun hierarchical structural films for effective wound healing, *Biomater. Adv.* 136 (2022), 212795.
- J. Hou, Y. Yang, D.-G. Yu, Z. Chen, K. Wang, Y. Liu, G.R. Williams, Multifunctional fabrics finished using electrosprayed hybrid Janus particles containing nanocatalysts, *Chem. Eng. J.* 411 (2021), 128474.
- Y. Cheng, Y. Xu, Y. Qian, X. Chen, Y. Ouyang, W.-E. Yuan, 3D structured self-powered PVDF/PCL scaffolds for peripheral nerve regeneration, *Nano Energy* 69 (2020), 104411.
- Q. Sun, Z. Yang, Z. Wang, L. Wu, Anti-fouling performance investigation of micron-submicron hierarchical structure PVDF membranes in water-in-oil emulsion separation, *J. Environ. Chem. Eng.* 10 (2022), 107497.
- F. Orudzhev, S. Ramazanov, D. Sobola, P. Kaspar, T. Trčka, K. Částková, J. Kastyl, I. Zvereva, C. Wang, D. Selimov, R. Gulakhmedov, M. Abdurakhmanov, A. Shuaibov, M. Kadiev, Ultrasound and water flow driven piezophototronic effect in self-polarized flexible $\alpha\text{-Fe}_2\text{O}_3$ containing PVDF nanofibers film for enhanced catalytic oxidation, *Nano Energy* 90 (2021), 106586.
- X. Yang, Y. Wang, X. Qing, A flexible capacitive sensor based on the electrospun PVDF nanofiber membrane with carbon nanotubes, *Sens. Actuat. A-Phys.* 299 (2019), 111579.
- C.-G. Lee, H. Javed, D. Zhang, J.-H. Kim, P. Westerhoff, Q. Li, P.J.J. Alvarez, Porous electrospun fibers embedding TiO_2 for adsorption and photocatalytic degradation of water pollutants, *Environ. Sci. Technol.* 52 (2018) 4285–4293.
- M. Wang, D. Fang, N. Wang, S. Jiang, J. Nie, Q. Yu, G. Ma, Preparation of PVDF/PVP core-shell nanofibers mats via homogeneous electrospinning, *Polymer* 55 (2014) 2188–2196.

- [47] X. Ji, R. Li, G. Liu, W. Jia, M. Sun, Y. Liu, Y. Luo, Z. Cheng, Phase separation-based electrospun Janus nanofibers loaded with Rana chensinensis skin peptides/silver nanoparticles for wound healing, *Mater. Des.* 207 (2021), 109864.
- [48] X. Zhou, S. Wu, C. Li, F. Yan, H. Bai, B. Shen, H. Zeng, J. Zhai, Piezophototronic effect in enhancing charge carrier separation and transfer in ZnO/BaTiO₃ heterostructures for high-efficiency catalytic oxidation, *Nano Energy* 66 (2019), 104127.
- [49] Y.R. Xie, Q.L. Ma, B. Yue, X.Y. Chen, Y. Jin, H.N. Qi, Y.L. Hu, W.S. Yu, X.T. Dong, H.L. Jiang, Triboelectric nanogenerator based on flexible Janus nanofiber membrane with simultaneous high charge generation and charge capturing abilities, *Chem. Eng. J.* 452 (2023), 139393.
- [50] B. Sarkara, W. Kweka, D. Verma, J. Kim, Effective vacuum residue upgrading using sacrificial nickel(II) dimethylglyoxime complex in supercritical methanol, *Appl. Catal. A-Gen.* 545 (2017) 148–158.
- [51] X.Z. Xu, M.X. Zhang, H. Lv, Y.J. Zhou, Y.Y. Yang, D.-G. Yu, Electrospun polyacrylonitrile-based lace nanostructures and their Cu (II) adsorption, *Sep. Purif. Technol.* 288 (2022), 120643.
- [52] M.J.C. Burgos, I.M.S. Roa, V. Fuenzalid, Synthesis of nanostructured BaTiO₃ films by hydrothermal modification of Ti surfaces using Ba(OH)₂ and oleic acid, *Chem. Phys. Lett.* 805 (2022), 139951.
- [53] J. Wu, N. Qin, D. Bao, Effective enhancement of piezocatalytic activity of BaTiO₃ nanowires under ultrasonic vibration, *Nano Energy* 45 (2018) 44–51.
- [54] H. Wang, X. Liu, S. Wang, L. Li, Dual templating fabrication of hierarchical porous three-dimensional ZnO/carbon nanocomposites for enhanced photocatalytic and photoelectrochemical activity, *Appl. Catal. B-Environ.* 222 (2018) 209–218.
- [55] Z. Zhu, P. Wu, G. Liu, X. He, B. Qi, G. Zeng, W. Wang, Y. Sun, F. Cui, Ultrahigh adsorption capacity of anionic dyes with sharp selectivity through the cationic charged hybrid nanofibrous membranes, *Chem. Eng. J.* 313 (2017) 956–966.
- [56] Y.M. Fu, Y.J. Wang, H.X. Zhao, Z.L. Zhang, B.N. An, C.Z. Bai, Z.Q. Ren, J.Z. Wu, Y. Q. Li, W.L. Liu, P. Li, J. Ma, Synthesis of ternary ZnO/ZnS/MoS₂ piezoelectric nanoarrays for enhanced photocatalytic performance by conversion of dual heterojunctions, *Appl. Surf. Sci.* 556 (2021), 149695.
- [57] X. Yin, W. Wu, F. Zhang, L. Li, J. Kou, C. Lu, Synergetic effect of piezoelectricity and heterojunction on photocatalytic performance, *J. Photoch. Photo A* 400 (2020), 112661.
- [58] R. Behera, K. Elanseralathan, Modeling of polyvinylidene fluoride nanocomposite utilizing BaTiO₃@SiO₂ for energy storage, *Mater. Today.: Proc.* 62 (2022) 6554–6560.
- [59] M.I. Litter, Heterogeneous photocatalysis: Transition metal ions in photocatalytic systems, *Appl. Catal. B-Environ.* 23 (1999) 89–114.
- [60] V. Subramanian, E.E. Wolf, P.V. Kamat, Influence of metal/metal ion concentration on the photocatalytic activity of TiO₂-Au composite nanoparticles, *Langmuir* 19 (2003) 469–474.
- [61] T.W.J. Albrecht, J. Addai-Mensah, D. Fornasiero, Critical copper concentration in sphalerite flotation: effect of temperature and collector, *Int. J. Miner. Process.* 146 (2016) 15–22.
- [62] Y. Chen, X. Deng, J. Wen, J. Zhu, Z. Bian, Piezo-promoted the generation of reactive oxygen species and the photodegradation of organic pollutants, *Appl. Catal. B-Environ.* 258 (2019), 118024.
- [63] D.V. Cuong, P.-C. Wu, L.-I. Chen, C.-H. Hou, Active MnO₂/biochar composite for efficient As(III) removal: insight into the mechanisms of redox transformation and adsorption, *Water Res.* 188 (2021), 116495.
- [64] D.-M. Guo, Q.-D. An, Z.-Y. Xiao, S.-R. Zhai, D.-J. Yang, Efficient removal of Pb(II), Cr(VI) and organic dyes by polydopamine modified chitosan aerogels, *Carbohydr. Polym.* 202 (2018) 306–314.
- [65] Y. Chen, Y. Liu, Y. Li, Y. Chen, Y. Wu, H. Li, S. Wang, Z. Peng, R. Xu, Z. Zeng, Novel magnetic pomelo peel biochar for enhancing Pb(II) And Cu(II) adsorption: Performance and mechanism, *Water Air Soil Poll.* 231 (2020) 404.
- [66] Q. Hou, H. Zhou, W. Zhang, Q. Chang, J. Yang, C. Xue, S. Hu, Boosting adsorption of heavy metal ions in wastewater through solar-driven interfacial evaporation of chemically-treated carbonized wood, *Sci. Total. Environ.* 759 (2021), 144317.
- [67] W.X. Zheng, Y.F. Tang, Z.W. Liu, G.X. Xing, K. Zhao, Enhanced charge carrier separation by bipiezoelectric effects based on pine needle-like BaTiO₃/ZnO continuous nanofibers, *J. Mater. Chem. A* 10 (2022) 13544.
- [68] X. Fan, X. Wang, Y. Cai, H. Xie, S. Han, C. Hao, Functionalized cotton charcoal/chitosan biomass-based hydrogel for capturing Pb²⁺, Cu²⁺ and MB, *J. Hazard. Mater.* 423 (2022), 127191.
- [69] H.B. Zhang, Y.Y. Liu, T. Chen, J.T. Zhang, J. Zhang, X.W. Lou, Unveiling the activity origin of electrocatalytic oxygen evolution over isolated Ni atoms supported on a N-Doped carbon matrix, *Adv. Mater.* (2019) 1904548.
- [70] H. Yang, A short review on heterojunction photocatalysts: Carrier transfer behavior and photocatalytic mechanisms, *Mater. Res. Bull.* 142 (2021), 111406.
- [71] J. Xie, R. Jin, A. Li, Y. Bi, Q. Ruan, Y. Deng, Y. Zhang, S. Yao, G. Sankar, D. Ma, J. Tang, Highly selective oxidation of methane to methanol at ambient conditions by titanium dioxide-supported iron species, *Nat. Catal.* 1 (2018) 889–896.
- [72] W. Wu, X. Yin, B.Y. Dai, J.H. Kou, Y.R. Ni, C.H. Lu, Water flow driven piezo-photocatalytic flexible films: Bi-piezoelectric integration of ZnO nanorods and PVDF, *Appl. Surf. Sci.* 517 (2020), 146119.
- [73] X.Y. Liu, L.B. Shen, W.X. Xu, W.Y. Kang, D.W. Yang, J.H. Li, S.H. Ge, H. Liu, Low frequency hydromechanics-driven generation of superoxide radicals via optimized piezotronic effect for water disinfection, *Nano Energy* 88 (2021), 106290.
- [74] Z.W. Seh, S. Liu, M. Low, S.-Y. Zhang, Z. Liu, A. Mlayah, M.-Y. Han, Janus Au-TiO₂ photocatalysts with strong localization of plasmonic near-fields for efficient visible-light hydrogen generation, *Adv. Mater.* 24 (2012) 2310–2314.
- [75] N. Kirkwood, B. Singh, P. Mulvaney, Enhancing quantum dot LED efficiency by tuning electron mobility in the ZnO electron transport layer, *Adv. Mater. Interfaces* 3 (2016) 1600868.